An assessment of SAPHIR calibration using quality tropical soundings

Gaëlle Clain, Hélène Brogniez, V. H. Payne, V. O. John, M. Luo

An Assessment of SAPHIR Calibration Using Quality Tropical Soundings

G. CLAIN* AND H. BROGNIEZ

Université Versailles St-Quentin, Sorbonne Universités, UPMC Université Paris 06, CNRS/INSU, LATMOS-IPSL, Guyancourt, France

V. H. PAYNE

Jet Propulsion Laboratory, California Institute of Technology, Pasadena, California

V. O. JOHN

Met Office Hadley Centre, Exeter, United Kingdom

M. LUO

Jet Propulsion Laboratory, California Institute of Technology, Pasadena, California

(Manuscript received 26 February 2014, in final form 1 August 2014)

ABSTRACT

The Sondeur Atmosphérique du Profil d'Humidité Intertropicale par Radiométrie (SAPHIR) instrument on board the Megha-Tropiques (MT) platform is a cross-track, multichannel microwave humidity sounder with six channels near the 183.31-GHz water vapor absorption line, a maximum scan angle of 42.96° (resulting in a maximum incidence angle of 50.7°), a 1700-km-wide swath, and a footprint resolution of 10 km at nadir. SAPHIR L1A2 brightness temperature (BT) observations have been compared to BTs simulated by the radiative transfer model (RTM) Radiative Transfer for the Television and Infrared Observation Satellite (TIROS) Operational Vertical Sounder (RTTOV-10), using in situ measurements from radiosondes as input. Selected radiosonde humidity observations from the Cooperative Indian Ocean Experiment on Intraseasonal Variability in the Year (CINDY)–Dynamics of the Madden–Julian Oscillation (DYNAMO) campaign (September 2011–March 2012) were spatiotemporally collocated with MT overpasses. Although several sonde systems were used during the campaign, all of the sites selected for this study used the Vaisala RS92-SGPD system and were chosen in order to avoid discrepancies in data quality and biases.

To interpret the results of the comparison between the sensor data and the RTM simulations, uncertainties associated with the data processing must be propagated throughout the evaluation. The magnitude of the bias was found to be dependent on the observing channel, increasing from 0.18 K for the 183.31 ± 0.2-GHz channel to 2.3 K for the 183.31 ± 11-GHz channel. Uncertainties and errors that could impact the BT biases were investigated. These can be linked to the RTM input and design, the radiosonde observations, the chosen methodology of comparison, and the SAPHIR instrument itself.

1. Introduction

As the most important greenhouse gas, water vapor has a major impact on the radiative balance of the earth. Understanding the atmospheric water cycle is critical for both weather and climate monitoring. The complexity of mechanisms governing the distribution of water vapor and clouds, and the range of scales involved require long-term observations with high temporal and spatial resolutions (Roca et al. 2010). Satellite observations can provide information on atmospheric water at the global scale. Observations in the infrared (IR), in the 6.3-μm band [e.g., by the Atmospheric Infrared Sounder (AIRS), the High-Resolution Infrared Radiation Sounder (HIRS), the first- and second-generation imagers of Meteosat, and the Cross-Track Infrared Sounder (CrIS)], are highly attenuated by clouds. Consequently, climatologies of

* Current affiliation: MODEM, Ury, France.

Corresponding author address: Hélène Brogniez, LATMOS, 11 Boulevard d'Alembert, 78280 Guyancourt, France.
E-mail: helene.brogniez@latmos.ipsl.fr

DOI: 10.1175/JTECH-D-14-00054.1

atmospheric relative humidity (RH) derived from IR observations are potentially subject to a clear-sky bias (Lanzante and Gahrs 2000; Fetzer et al. 2006; John et al. 2011; Yue et al. 2013). Some analyses yield to include low cloud scenes for the free-tropospheric humidity estimation; these clouds having a negligible impact on the 6.3-μm radiances, which helps to increase the sampling (Brogniez et al. 2006). Microwave (MW) observations around 183.31 GHz, on the other hand, are only affected by optically thick or precipitating clouds and thus allow for extension of studies of the water vapor distribution to a wider range of atmospheric conditions (Hong et al. 2005a,b). Microwave observations of water vapor in the upper and free troposphere are also available from polar-orbiting satellite instruments, such as the Microwave Humidity Sounders (MHS) on board the European Organisation of the Exploitation of Meteorological Satellites (EUMETSAT) Meteorological Operation (MetOp) satellites, the Advanced Microwave Sounding Unit-B (AMSU-B) sensors on board the National Oceanic and Atmospheric Administration (NOAA) satellites, and the Defense Meteorological Satellite Program (DMSP) Special Sensor Microwave Imager/Sounders (SSM/IS) (Spencer and Braswell 1997; Buehler and John 2005).

Dedicated to improving the documentation of the water and energy cycles in the tropical belt, the Indo-French satellite Megha-Tropiques (MT) was launched in October 2011. It is the result of a strong collaboration between the Indian Space Research Organisation (ISRO) and the French Centre National d'Etudes Spatiales (CNES). With a relatively high orbit (867 km) and a slight inclination of 20° relative to the equatorial plane, it provides a unique sampling of the tropical belt, with up to six overpasses per day near 12°N/S (Desbois et al. 2007). The SAPHIR (Sondeur Atmosphérique du Profil d'Humidité Intertropicale par Radiométrie; Eymard et al. 2002) instrument on board the MT platform has six channels distributed around the 183.31-GHz water vapor line, providing enhanced information on the vertical distribution of water vapor compared to the use of the three channels available on MHS and AMSU-B (Brogniez et al. 2013; Gohil et al. 2013). This, combined with the unique sampling, enables SAPHIR to provide an extensive picture of RH in the tropics.

In addition, the low-inclination orbit of MT allows a relatively large number of coincident observations with other sensors in higher-inclination orbits, providing excellent opportunities for calibration. For example, the definition of a constellation of sensors is key to the success of the National Aeronautics and Space Administration (NASA) Global Precipitation Measurement (GPM) mission. Moreover, the GPM Intercalibration Working Group (XCAL) has included SAPHIR in its efforts to develop calibration adjustments among existing microwave radiometers (Wilheit et al. 2013).

Before the data can be utilized in studies of the environment, the calibration and evaluation of the satellite sensor system are essential. The radiometric sensitivity of any sensor must be established both before and after launch. The actual performance may differ from prelaunch estimations. It is thus particularly important to validate the in-flight performance of the sensor.

One approach for validation of in-flight performance is to perform comparisons between the sensor measurements and calculations from a radiative transfer model (RTM), using in situ measurements from radiosondes as input to the RTM (e.g., Fetzer et al. 2003; Tobin et al. 2006). While radiosonde humidity measurements are subject to their own uncertainties, they often represent the best available knowledge of the atmospheric state and are frequently considered a reference.

However, the comparison between the sensor data and the reference data is not always straightforward, and uncertainties associated with the data processing must be propagated throughout the evaluation (e.g., Kottayil et al. 2012; Moradi et al. 2013). The potential sources of uncertainty are linked to the methodological approach, to the RTM inputs, including the uncertainties affecting the reference (radiosonde) data, and to the design of the RTM used to perform the comparison.

The scope of this paper is to evaluate the measurements performed by SAPHIR at the brightness temperature (BT) level using a uniform set of tropical radiosonde RH observations. Section 2 describes the SAPHIR observations, the radiosonde reference dataset, and the methodology used in the comparisons. Section 3 presents the BT simulations and discusses the performance of the radiative transfer model. In section 4, the biases are described. The factors that can influence the BT biases are identified and evaluated to the extent possible. Section 5 provides the summary, a discussion of the results, and some conclusions.

2. Humidity observations

a. *SAPHIR observations*

SAPHIR is a cross-track radiometer that observes the earth with a maximum scan angle of 42.96°, a 1700-km-wide swath, and a footprint resolution of 10 km at nadir that stretches into a 14 km × 22 km ellipse on the edges of the swath. The characteristics of the instrument are summarized in Table 1 (adapted from Karouche et al. 2012).

SAPHIR calibration is performed on board, against a hot target (at about 290 K) and against cold space (2.7 K). To reach the required radiometric sensitivity indicated in Table 1, with the specified resolution of 10 km at nadir, data are oversampled in the cross-track

TABLE 1. Radiometric on-ground and in-orbit performance of SAPHIR channels (adapted from Karouche et al. 2012).

Channels	Central frequency (GHz)	Bandwidth (MHz)	Radiometric sensitivity NeΔT (K) (on ground/in orbit)
C1	183.31 ± 0.2	200	1.52/1.44
C2	183.31 ± 1.1	350	1.09/1.05
C3	183.31 ± 2.8	500	0.95/0.91
C4	183.31 ± 4.2	700	0.82/0.77
C5	183.31 ± 6.8	1200	0.66/0.63
C6	183.31 ± 11	2000	0.56/0.54

direction. For each scan line and each channel, 182 samples are collected (L1A data). The L1A data are resampled to obtain 130 nonoverlapping pixels (L1A2 data). While the pixels of L1A2 data are contiguous across track, some overlap exists in the along-track direction. With geophysical variables (L2 data; such as RH profiles) being produced from the L1A2 level, the focus is on evaluating of the latter in order to help the propagation of the results directly onto the L2.

Hereafter, SAPHIR channels will be referred to as C1–C6, with respect to Table 1 specifications. Table 1 shows both the prelaunch and the postlaunch radiometric sensitivities (Karouche et al. 2012), demonstrating the high quality of the performance of the instrument. The radiometric sensitivities range from 1.52 K for C1 to 0.5 K for C6. These values correspond to the standard deviation of the instrument signal output and are an inverse function of the bandwidth. Assuming that the instrument noises are normally distributed, then the noise equivalent differential temperature (NeΔT) is the standard deviation of the distribution (i.e., the accurate observed values have a 68% probability of falling in an interval twice as wide as the NeΔT). Therefore, we define the uncertainty associated with the instrument sensitivity ε_{is} as

$$\varepsilon_{is} = \mathrm{Ne}\Delta\mathrm{T} \quad (\mathrm{K}). \tag{1}$$

This study relies on purely cloud-free scenes identified in version 1.05 of the L1A2 data. In the 183-GHz region, contamination by nonscattering clouds (no precipitating particles associated with deep convective clouds or cirrus anvil clouds) is negligible. However, radiative transfer (RT) simulations of cloudy atmospheres require profiles of liquid and ice water content. These are not provided by conventional radiosounding probes. Scenes with deep convective clouds, convective overshooting, and precipitation were rejected following the method stated in Hong et al. (2005a). This method relies on the fact that for sufficiently large particles, scattering will produce a change of sign with respect to the arrangement of the BTs for a clear-air situation (C1 < C2 < C3 < C4 < C5 < C6). The Hong et al. cloud screening approach has previously been validated against aircraft microwave and radar observations from two different tropical campaigns. Remaining cloudy scenes were identified directly from the radiosonde observations: RH profiles with more than four measurements above 95% RH were arbitrarily discarded from the database. This restrictive RH filter provides similar results to the method applied in Buehler at al. (2004) that interprets strong depressions in the 183.3 ± 7-GHz BTs of AMSU-B as a cloud signal. Finally, daytime and nighttime observations were determined using the solar elevation angle for each radiosounding.

b. *Radiosonde observations during CINDY–DYNAMO*

The Cooperative Indian Ocean Experiment on Intraseasonal Variability in the Year (CINDY)–Dynamics of the Madden–Julian Oscillation (DYNAMO; CD) international field campaign took place over the Indian Ocean between September 2011 and March 2012. The primary objectives of this campaign were to investigate key processes involved in the initiation of the Madden–Julian oscillation (MJO) and to improve the simulation and prediction of MJO events (for further information on CINDY in the Year 2011 (CINDY2011), see http://www.jamstec.go.jp/iorgc/cindy/; for information on DYNAMO, see http://www.eol.ucar.edu/projects/dynamo/). This campaign involved a radar network (island and shipborne radars), a ship/mooring network, a few in situ measurements from aircraft (microphysics probes and radar), and an atmospheric sounding network during three observing periods (special, intensive, and extended). The campaign was supplemented by other experiments, such as the Atmospheric Radiation Measurement Program (ARM) MJO Investigation Experiment (AMIE). Overall, more than 10 000 high-resolution soundings were collected from the 51 priority sounding sites, covering a domain spanning 120° in longitude (eastern Africa to the western Pacific; Ciesielski et al. 2014).

For this study, only the so-called level 3 of the CD radiosounding measurements performed over 10 enhanced sonde sites were used (Table 2, includes the three-letter abbreviation for each site; in the following, these abbreviations will be used.) Figure 1 shows the geographic distribution of the selected sites. For these sites, the processing errors and various biases had been identified and corrected when possible. The dataset includes one continental site, seven islands (referred to as oceanic sites), and two research vessels (R/V). The raw measurements (or level 0) files underwent format conversion (level 1), an automated quality control procedure with the Atmospheric Sounding Processing Environment

TABLE 2. Description of CINDY–DYNAMO level 3 database.

Site name	Full site name	Country–location	Elev (m)	Lat (°N)	Lon (°E)	Site type	Dry bias correction
BAR	*Baruna Jaya*	Indonesia	3.0	−7 to −6.43	95–99.52	R/V	NRBC
DAR	Darwin	Australia	30.0	−12.42	130.9	Continental	NRBC
DIE	Diego Garcia	United Kingdom	2.0	−7.31	72.42	Oceanic	NRBC
GAN	Gan Island	Maldives	1.0	−0.69	73.15	Oceanic	Vaisala
MAL	Male	Maldives	2.0	4.19	73.53	Oceanic	Vaisala
NAU	Nauru	Nauru Island	4.0	−0.52	166.92	Oceanic	NRBC
ROG	*Roger Revelle*	United States	19.0	−29.85 to 4.88	36.39–91.45	R/V	NRBC
SEY	Seychelles	Seychelles	4.0	−4.68	55.53	Oceanic	NRBC
SIP	Sipora	Indonesia	7.0	−2.03	99.59	Oceanic	NRBC
MAN	Manus	Manus Island	4.0	−2.060	147.430	Oceanic	Vaisala

(ASPEN) (Ciesielski et al. 2012) software (level 2), and finally error and bias corrections (level 3).

Although several sonde systems were used during the campaign (Mesei, Graw, Modem, and Sippican Mark), all of the 10 enhanced sonde sites selected for this study used the Vaisala RS92 system. These were chosen in order to avoid discrepancies in data quality and biases. A recent paper by Moradi et al. (2013) comparing several radiosonde types to AMSU-B and MHS microwave observations argues in favor of the reliability of Vaisala probes in the mid- to upper troposphere. Those sondes are widely used for research and operational purposes, and their errors and uncertainties are well documented (Miloshevich et al. 2004, 2006, 2009; Vömel et al. 2007; Nash et al. 2011). The RS92 RH measurements are known to be affected by the following issues:

- During daytime, the solar heating of the sensor induces a dry bias, which is mainly a function of the solar elevation angle and of the cloud cover. Comparisons against references have shown that this error lies between 9% at the surface and about 50% in the upper troposphere (~15 km). The magnitude of the bias depends on RH.
- The slow sensor response to humidity changes at low temperature (<−45°C) necessitates a time lag correction. The time lag is particularly evident in regions of the atmosphere where humidity gradients are steep, such as at the tropopause and in regions above and below cirrus layers. The time lag results in a distortion of the profile. The correction is generally temperature dependent.
- A sensor random production variability related to humidity conditions, leading to an uncertainty of ±1.5% of the measured RH for RH > 10% and ±3% of the measured RH for RH < 10%.
- A residual uncertainty bias accounting for both sensor and ground check calibration variability. This uncertainty bias differs between daytime ± (5% of the measured RH + 0.5% offset) and nighttime ± (4% of the measured RH + 0.5% offset).

A dry bias correction was applied to the daytime observations. For all but three sites, the dry bias correction applied was based on the algorithm used by the Global Climate Observing System (GCOS) Reference Upper-Air Network (GRUAN) community (Seidel et al. 2009). This algorithm, referred to as the National Center for Atmospheric Research (NCAR) radiation bias correction (NRBC), is described in Wang et al. (2013). For the GAN, MAL, and MAN sites, the dry bias correction was performed with the Vaisala dedicated acquisition software DigiCORA III. The Vaisala dry bias correction also accounts for time lag error. In addition to dry bias and time lag corrections, the NRBC correction accounts for calibration uncertainties (Wang et al. 2013). The daytime and nighttime observations constitute 55% and 45% of the database, respectively. Figure 2 shows that the GAN and MAN sites account for just over half of the database in terms of the number of collocations. Therefore, the database is approximately equally distributed between the two types of radiative corrections

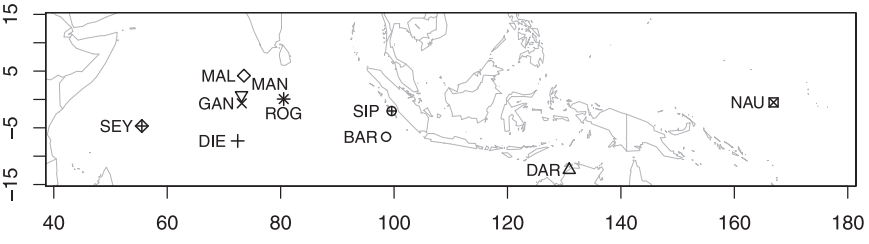

FIG. 1. Geographic distribution of the selected CD sites (adapted from Ciesielski et al. 2014).

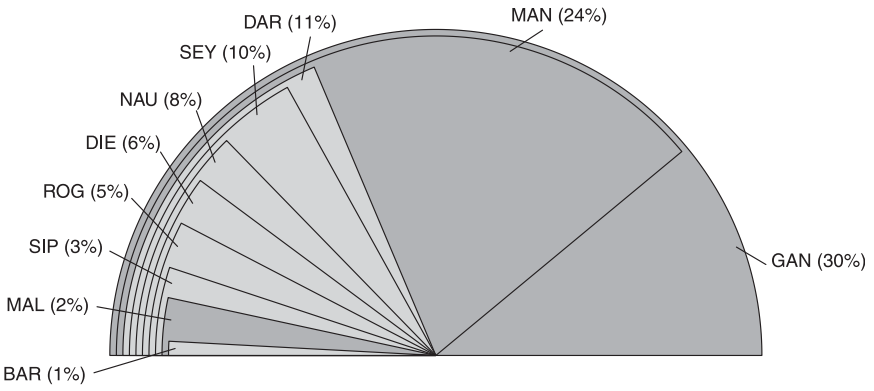

FIG. 2. Relative contribution of each site to the total number of collocations, including both daytime and nighttime collocations. The light shading corresponds to the NCAR bias correction and the dark shading corresponds to the Vaisala correction.

on daytime observations. Radiosoundings performed on board scientific ships were corrected for the temperature perturbation induced by the metallic body of the ship at surface levels (Yoneyama et al. 2002). The nighttime observations underwent a radiative correction for temperature that also accounts for time lag error.

For each radiosonde profile, we identified the closest SAPHIR pixel to the radiosonde launch site in a 50-km-radius area and within in a time window of ±45 min between the radiosonde launch time and the SAPHIR observation. Among the 5981 recorded Vaisala RS92 radiosoundings of CD, 194 of them qualified as spatio-temporal collocations with Megha-Tropiques in clear-sky conditions. Figure 3 shows the mean profiles of temperature and RH of the 194 profiles together with their standard deviations, alongside the Interim European Centre for Medium-Range Weather Forecasts (ECMWF) Re-Analysis (ERA-Interim) profiles averaged over the tropical belt (±30° in latitude) for 2011 (Berrisford et al. 2009). As expected from prior knowledge of tropical climate (e.g., Peixoto and Oort 1996), the temperature profile is close to being invariant, and is very similar in the two

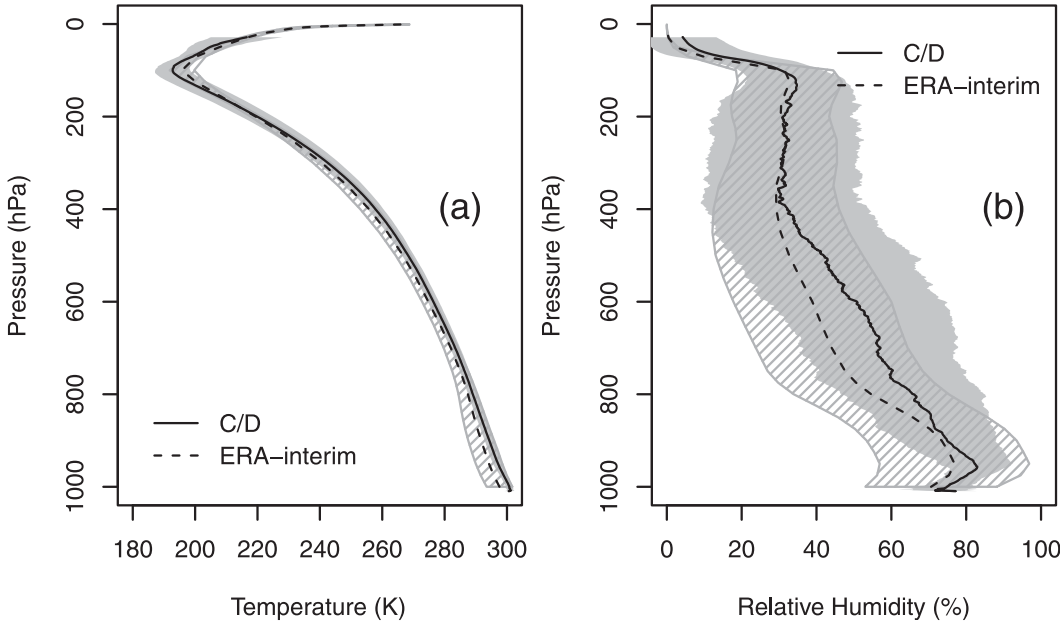

FIG. 3. (a) Mean temperature and (b) RH profiles of the CD sites (black line) and their associated standard deviation (gray shading). The corresponding profiles from ERA-Interim, sampled over the tropics (±30° around the equator) for year 2011, are also indicated (mean: dashed lines, standard deviation: hatched areas).

sets. The CD RH profiles exhibit a slightly moister midtroposphere (400–850 hPa) than the ERA-Interim for the entire tropical belt, probably induced by the strong convective activity of this part of the tropics. The difference between the CD and ERA-Interim mean RH profiles is well within the ERA-Interim variability.

3. Simulations of SAPHIR BTs

a. RTTOV-10 simulations

The Radiative Transfer for the Television and Infrared Observation Satellite (TIROS) Operational Vertical Sounder (RTTOV) model was developed for numerical weather prediction (NWP) purposes at the ECMWF, where it is used operationally. RTTOV (Saunders et al. 1999) is a regression-based fast radiative transfer model: the model optical depths are computed as a linear combination of profile predictors (i.e., temperature, pressure, zenith angle, and absorber amount).

The linear coefficients are derived from regressions based on accurate line-by-line (LBL) simulations of a wide range of atmospheric profiles. The channel-averaged transmittances for microwave sensors are calculated with the AMSU transmittance (AMSUTRAN) model (Saunders et al. 2012), which uses a version of the Liebe-89 (Liebe 1989) Millimeter-Wave Propagation Model (MPM) for water vapor and MPM-92 for dry air (Liebe et al. 1992). The AMSUTRAN code for mixed gases is based on the Liebe MPM-93 (Liebe et al. 1993) model with coefficients from MPM-92 and combines MPM-93 and coefficients from High Resolution Transmission (HITRAN) for ozone. Water vapor is the only gas allowed to vary in the simulations. Oxygen (O_2), ozone (O_3), and nitrogen (N_2) are considered well-mixed gases.

The radiosonde pressure, temperature, and specific humidity profiles were used as inputs to RTTOV-10 in order to simulate SAPHIR BTs. The correct zenith angle was extracted from SAPHIR observation data after the collocation stage, and the surface emissivity was either taken from the Prigent et al. (2006, 2008) atlas for continental surfaces or calculated internally by the Fast Emissivity Model, version 4 (FASTEM-4), model (English and Hewison 1998) over oceanic surfaces.

b. RTM evaluation

1) RTMs DESCRIPTION

The performance of RTTOV-10 has been studied by the Satellite Application Facility for Numerical Weather Prediction (NWP SAF) for IR instruments such as AIRS and Infrared Atmospheric Sounding Interferometer (IASI; Saunders et al. 2012). For the purpose of the present paper, the evaluation of RTTOV-10 with respect to the MPM has been performed by NWP SAF under simplified assumptions: the calculations involved a plane-parallel atmosphere, meaning no Earth curvature nor refraction, three different scan angles (i.e., nadir, 27°, and 60°), and two different sets of atmospheric profiles (an 83-profile-dependent training set and a 52-profile-independent set) defined on the 51 levels of RTTOV. In all cases, the mean difference between MPM and RTTOV-10 was less than 0.1 K and the standard deviation was less than 0.3 K (NWP SAF report available from http://research.metoffice.gov.uk/research/interproj/nwpsaf/rtm/rtm_rttov10.html).

Moreover, previous versions of RTTOV have been compared to several LBL models for AMSU-B and MHS water vapor channels. The RTTOV–LBL differences were found to be very small (Chen et al. 2010). A comparison exercise by Buehler et al. (2006) showed that mean differences between RTTOV-7 and the Atmospheric Radiative Transfer Simulator (ARTS) model (described further in this section) over an idealized oceanic situation ranged from 0.014 to 0.104 K for simulations of AMSU-B channels 18–20. The larger discrepancies were attributed to the transmittance parameterization of this version of RTTOV. More recently, Chen et al. (2010) investigated water vapor regression methods in fast radiative transfer models and compared LBL to fast RTMs in the microwave region. The BT bias between the LBL and fast RTMs was less than 0.1 K on average for MHS channels 3–5 and was highly stable in humid conditions. These statistics, while not reflecting the actual performance of RTTOV-10, give an idea of the ability of recent RTMs to simulate 183.31-GHz BTs.

To evaluate the uncertainty associated with RTTOV-10 simulations, two different LBL models were used here to simulate SAPHIR BTs on the same radiosonde dataset: the ARTS model (Buehler et al. 2005; Eriksson et al. 2011) and the monochromatic radiative transfer (MonoRTM) model (Payne et al. 2011; Clough et al. 2005).

The ARTS model, described in detail in Buehler et al. (2005) and Eriksson et al. (2011), is an LBL RTM that simulates radiances in the IR and MW spectral ranges. The computations can be tuned using a set of models for the continuum, listed in Buehler et al. (2005). For this study, gaseous absorption was assumed to be due to only water vapor, ozone, oxygen, and nitrogen. The absorption models used were that of Rosenkranz (1998) for water vapor and O_2 and that of Rosenkranz (1993) for N_2. Monochromatic calculations were performed for 11 frequencies inside the passbands, and the results were convolved with the sensor passband response, which was assumed to be rectangular.

MonoRTM has been extensively validated using ground-based measurements from the Department of Energy's

TABLE 3. Statistical elements of the comparison between SAPHIR BTs simulated by RTTOV-10, ARTS, and MonoRTM: correlation coefficient (R), mean BT difference, standard deviation (σ), and slope of linear fit.

	C1	C2	C3	C4	C5	C6
$R_{\mathrm{RTTOV,ARTS}}$	0.94	0.97	0.98	0.98	0.98	0.98
$\langle \mathrm{RTTOV} - \mathrm{ARTS} \rangle$ (K)	−0.04	0.21	0.44	0.44	0.51	0.68
$\sigma_{\mathrm{RTTOV,ARTS}}$ (K)	1.78	1.09	0.85	0.79	0.76	0.77
$\mathrm{Slope}_{\mathrm{RTTOV,ARTS}}$ ($\mathrm{K\,K^{-1}}$)	0.91	0.98	0.96	0.95	0.94	0.92
$R_{\mathrm{RTTOV,MonoRTM}}$	0.94	0.99	0.99	0.99	0.99	0.99
$\langle \mathrm{RTTOV} - \mathrm{MonoRTM} \rangle$ (K)	−1.50	−0.60	0.20	0.18	0.04	−0.44
$\sigma_{\mathrm{RTTOV,MonoRTM}}$ (K)	1.68	0.64	0.38	0.33	0.32	0.31
$\mathrm{Slope}_{\mathrm{RTTOV,MonoRTM}}$ ($\mathrm{K\,K^{-1}}$)	0.95	1.01	1.01	1.01	1.02	1.02
$R_{\mathrm{ARTS,MonoRTM}}$	0.98	0.98	0.99	0.99	0.99	0.98
$\langle \mathrm{ARTS} - \mathrm{MonoRTM} \rangle$ (K)	−1.37	−0.79	−0.23	−0.25	−0.46	−1.12
$\sigma_{\mathrm{ARTS,MonoRTM}}$ (K)	1.11	0.95	0.73	0.69	0.66	0.68
$\mathrm{Slope}_{\mathrm{ARTS,MonoRTM}}$ ($\mathrm{K\,K^{-1}}$)	1.03	0.99	1.02	1.03	1.05	1.07

ARM (Clough et al. 2005; Cadeddu et al. 2007; Payne et al. 2008, 2011; Cimini et al. 2009). MonoRTM version 4.0 onward may be used from the MW to the ultraviolet, with cloud liquid water in the MW. For the calculations performed in this work, we used MonoRTM version 4.2. Spectral line parameters are based on HITRAN 2004 with a few selected exceptions, namely, the parameters for the oxygen lines and for the four strong water vapor lines at 22, 183, 325, and 380 GHz. The line strengths for the 22- and 183-GHz water vapor lines are based on an analysis of Stark effect measurements described in Clough et al. (1973). The temperature dependences of the half-widths and the pressure shifts for these four water lines are from Gamache's calculations, which are described in Payne et al. (2008). MonoRTM uses the Mlawer, Tobin, Clough, Kneizys, and Davies (MT_CKD) continuum model (Mlawer et al. 2012; Clough et al. 2005), which includes contributions from self- and foreign-broadened water vapor, N_2, O_2, and O_3, although the O_3 continuum is not significant in the microwave region.

2) COMPARISON OF RTM SIMULATIONS

The collocated database discussed in section 2b was used as input into the RTTOV, ARTS, and MonoRTM models to simulate what SAPHIR would have measured. The mean, standard deviation, and correlations computed from comparisons between the three models are listed in Table 3. The three models clearly agree on the simulation of SAPHIR channels. Table 3 shows that the mean differences between RTTOV-10 and ARTS simulations range from close to 0 K (for C1) to 0.7 K for C6, with RTTOV-10 being consistently warmer than ARTS. The standard deviation between the two models is larger for C1 (1.78 K) than for the other channels, but the correlations between the two simulations are high and the slopes are close or equal to unity for all channels. The correlation between the MonoRTM and RTTOV-10 simulations is 0.94 for C1 and 1.0 for C2–C6. The standard deviation of the RTTOV–MonoRTM difference peaks for C1 with 1.7 K and decreases to 0.3 K for C5 and C6. The slope values range between 0.95 $\mathrm{K\,K^{-1}}$ for C1 and 1.01 $\mathrm{K\,K^{-1}}$ for C2–C4. For C1 (C2, C6), MonoRTM is 1.5 K (0.54, 0.42 K) warmer on average than RTTOV-10. For C3–C5, the differences are close to 0.

The difference between the Rosenkranz and Liebe models in ARTS and RTTOV was previously evaluated in Buehler et al. (2006). Differences are lower than 0.5 K in tropical regions. Table 3 shows that the two LBL models differ most for C1 and C6. For these channels, the absolute difference is greater than 1 K. While the discrepancy for C6 can be potentially linked to differences in the water vapor continuum in the models [see section 4b(1)], the difference observed in C1 requires further investigation.

This comparison between ARTS, MonoRTM, and RTTOV-10 was used to estimate the BT difference that arises between different types of RTMs. We define an RTM error ε_m that applies to each channel of SAPHIR using the mean difference between an average of the two LBL simulations and RTTOV-10's BTs, written as

$$\varepsilon_m = \langle \mathrm{RTTOV} - \langle \mathrm{ARTS, MonoRTM} \rangle \rangle \quad (\mathrm{K}), \qquad (2)$$

where $\langle$ARTS, MonoRTM$\rangle$ is the mean of the BTs simulated by the two LBL models.

Figure 4 shows that the set of average values between ARTS and MonoRTM SAPHIR BTs is in good statistical agreement with the RTTOV-10 simulations. The correlation coefficient for all channels is close to 1.0 and slopes range between 0.92 $\mathrm{K\,K^{-1}}$ for C1 and 1 K for C2. The dispersion is larger for C1 (1.8 K) and decreases to 0.5 K for C3–C6.

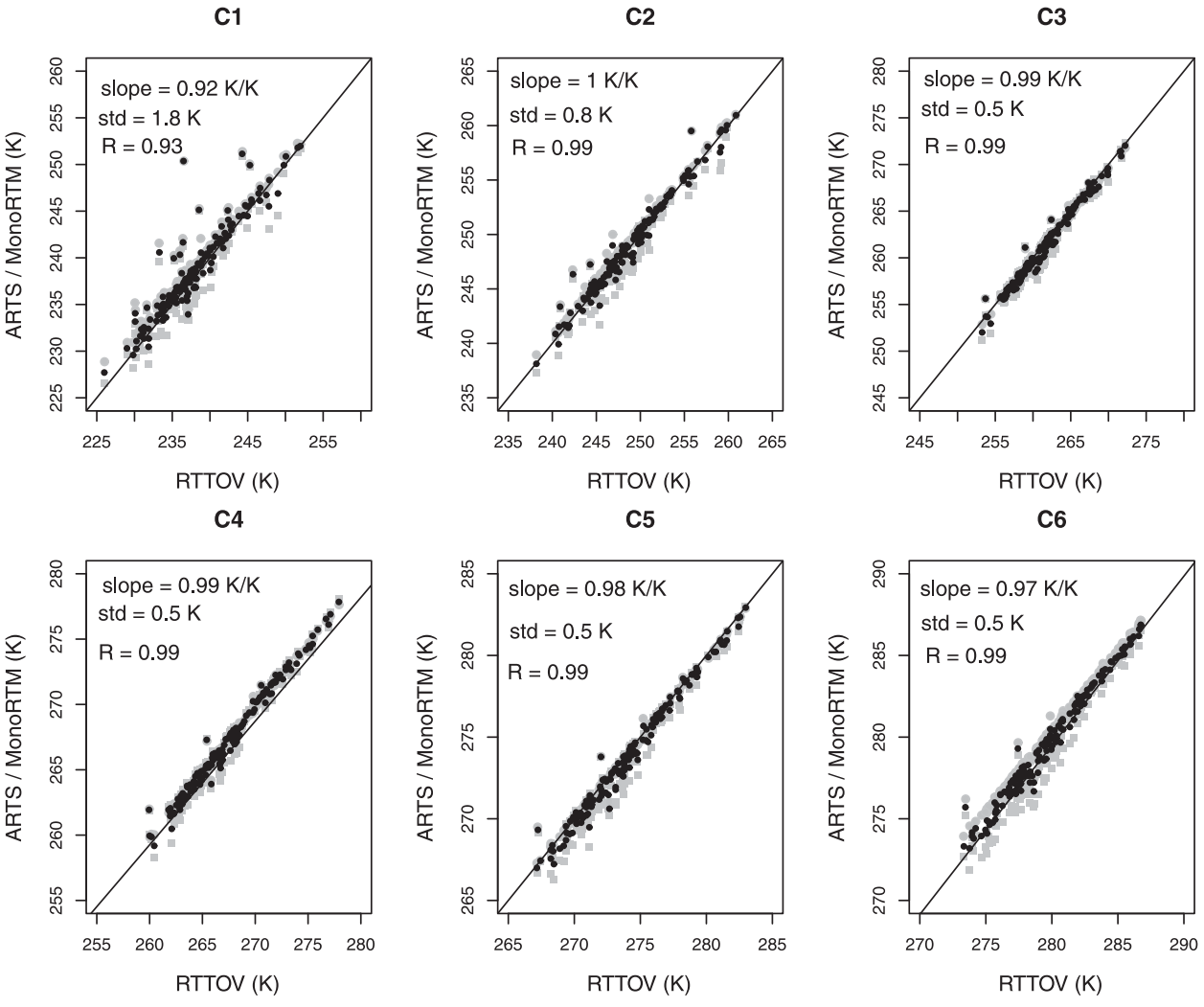

FIG. 4. SAPHIR BTs simulated by RTTOV-10 (horizontal axes) vs ARTS and MonoRTM (gray squares and diamonds, respectively) and the mean of the two LBL RTMs (black dots). The slope, standard deviation, and correlation coefficient between the latter and RTTOV-10 simulations are displayed for each SAPHIR channel.

4. Analyses of the biases

a. Main features of the BT bias

The collocated radiosonde humidity profiles were used to simulate RTTOV-10 BTs and the simulated BTs were compared to SAPHIR observations. The simulated-minus-observed BTs (called "bias") were calculated for each collocated sounding. The mean, standard deviation, linear fit slopes, and correlation coefficients are listed in Table 4. A one-sample *t* test (Student 1908) was applied to test, for each case, whether the biases were significantly different from 0 (defined as the null hypothesis). The *p* values of the *t* tests are provided in Table 4. They must be lower than 0.05 to reject the null hypothesis (at the 95% confidence interval).

The following features characterize the simulated-minus-observed BT bias for all data subsets evaluated from a single SAPHIR pixel (Table 4):

- A warm bias in the simulations for C1–C6, showing a temperature-dependent pattern: the bias amplitude increases with temperature, from 0.18 K for C1 to 2.26 K for C6.
- A strong correlation coefficient for all channels and all data subsets greater than 0.87.
- Slopes of linear fit between observations and simulated BTs are close to unity for all channels.

The statistics reported in Table 4 were calculated using first, the whole dataset, then splitting the dataset between daytime and nighttime observations. The bias

TABLE 4. Simulated minus observed BT bias statistical elements: means, p values from a Student's t test, standard deviations (σ), correlation coefficients, and slopes of linear fit.*

	Pixels		C1	C2	C3	C4	C5	C6
Day + night	1	Bias (K)	0.18	0.76	1.28	1.58	1.48	2.26
		p value	0.25	1×10^{-12}	$<2 \times 10^{-16}$	$<2 \times 10^{-16}$	$<2 \times 10^{-16}$	$<2 \times 10^{-16}$
		σ (K)	2.13	1.38	0.98	0.85	0.83	0.77
		R	0.91	0.96	0.97	0.98	0.98	0.98
		Slope (K K^{-1})	0.99	1.01	0.96	0.94	0.93	0.91
	25	Bias (K)	0.19	0.75	1.30	1.59	1.53	2.31
		p value	0.14	1×10^{-15}	$<2 \times 10^{-16}$	$<2 \times 10^{-16}$	$<2 \times 10^{-16}$	$<2 \times 10^{-16}$
		σ (K)	1.85	1.19	0.87	0.80	0.83	0.92
		R	0.93	0.97	0.98	0.98	0.98	0.97
		Slope (K K^{-1})	1.04	1.04	0.96	0.94	0.92	0.88
Day	1	Bias (K)	0.55	1.05	1.43	1.69	1.65	2.34
		p value	0.03	3×10^{-11}	$<2 \times 10^{-16}$	$<2 \times 10^{-16}$	$<2 \times 10^{-16}$	$<2 \times 10^{-16}$
		σ (K)	2.53	1.46	0.95	0.79	0.78	0.74
		R	0.87	0.95	0.98	0.98	0.98	0.98
		Slope (K K^{-1})	0.94	0.98	0.96	0.95	0.93	0.93
	25	Bias (K)	0.64	1.01	1.44	1.71	1.66	2.45
		p value	6×10^{-4}	3×10^{-13}	$<2 \times 10^{-16}$	$<2 \times 10^{-16}$	$<2 \times 10^{-16}$	$<2 \times 10^{-16}$
		σ (K)	1.91	1.24	0.88	0.77	0.75	0.81
		R	0.93	0.97	0.98	0.98	0.98	0.98
		Slope (K K^{-1})	1.01	1.02	0.95	0.94	0.93	0.89
Night	1	Bias (K)	−0.41	0.38	1.09	1.43	1.29	2.16
		p value	0.03	3×10^{-3}	$<2 \times 10^{-16}$	$<2 \times 10^{-16}$	$<2 \times 10^{-16}$	$<2 \times 10^{-16}$
		σ (K)	1.76	1.19	0.98	0.89	0.85	0.79
		R	0.94	0.97	0.97	0.98	0.97	0.98
		Slope (K K^{-1})	1.01	1.03	0.95	0.93	0.93	0.89
	25	Bias (K)	−0.36	0.43	1.13	1.44	1.36	2.14
		p value	0.04	3×10^{-4}	$<2 \times 10^{-16}$	$<2 \times 10^{-16}$	$<2 \times 10^{-16}$	$<2 \times 10^{-16}$
		σ (K)	1.61	1.06	0.83	0.83	0.89	1.01
		R	0.95	0.97	0.98	0.98	0.97	0.96
		Slope (K K^{-1})	1.07	1.06	0.98	0.95	0.92	0.86

* The p value should be lower than 0.05 (the 95% confidence interval) to reject the null hypothesis (difference equals 0). The dataset is divided into three subsets: day + night, day-only, and night-only conditions. For each subset, the observed BT from the single or an average upon the 5 × 5 closest pixels from the sounding launch site is used.

was computed using SAPHIR BTs either from a single pixel or from an average around the target area. These calculations were performed with the aim of identifying any possible bias source. Further discussion is provided in the subsections that follow.

b. *Discussion on the sources of uncertainties and biases*

The factors that can influence the bias are related to the methodology and can be linked specifically to the radiative transfer model, to the radiosonde observations, and to the SAPHIR instrument itself.

1) ERRORS LINKED TO THE RADIATIVE TRANSFER MODEL

Ozone is one of several factors impacting the simulations near the 183.31-GHz absorption line. The result of inclusion of O_3 in the model is a slight cooling of modeled BT in that reaches 0.5 K in AMSU channel 18 and is at least one order of magnitude lower for other channels (John and Buehler 2004). MonoRTM simulations were performed to quantify the impact of O_3 on the SAPHIR channels. Two sets of simulations—with and without ozone—were performed for a tropical standard atmosphere, for a zenith angle of 42°. The differences are shown in Fig. 5. Absorption by O_3 impacts C2 significantly but C6 only marginally. The integrated BT difference over the C2 bandwidth ranges

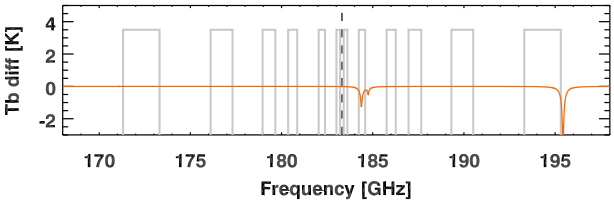

FIG. 5. The BT difference between simulations with MonoRTM, including ozone minus simulations without ozone (orange line) for a tropical standard atmosphere and zenith angle of 42°. The gray boxes show the SAPHIR channels' positions and widths.

between 0.3 K at nadir to 0.5 K at 42°, in agreement with John and Buehler (2004). For drier atmospheres and scan angles farther from nadir, the differences can be even larger (not shown). For C6, the mean effect is small, about 0.05 K. This exercise shows the minor impact of ozone in SAPHIR simulations assuming top-hat transfer functions.

The impact of absorption by ozone on the BTs, restricted to C2 and C6, is defined as ε_{O_3} and is expressed in terms of BTs instead of radiances for simplification,

$$\varepsilon_{O_3} = \sum_{\nu} (BT_{O_3} - BT_{\not{O}_3}), \tag{3}$$

where ν refers to the frequency windows of C2 and C6.

Since the SAPHIR weighting functions cover the free troposphere (see Fig. 2 of Brogniez et al. 2013) for a tropical standard atmosphere, with a deeper sounding for a drier atmosphere, the surface emissivity could also affect the simulations. According to Aires et al. (2011), who investigated the impact of the choice of emissivity on AMSU-A and AMSU-B channels, the mean effect of emissivity in channels similar to C2 and C3 is close to zero in the RTTOV-10 model. An additional sensitivity test with RTTOV-10 on the CD dataset confirms that surface emissivity only affects C4–C6, and by less than 10^{-2} K (fixed profiles with two prescribed emissivities of 0.5 and 0.9).

Finally, the larger bias for C6 raises the question of the impact of the water vapor continuum in the 183.31 (±11)-GHz channel, which is strongly asymmetric. Indeed, the water vapor absorption spectrum differs significantly at 194.31 and 172.31 GHz. Although the impact of the representation of the water vapor continuum on the MW simulations is beyond the scope of this work, its evaluation is an important question to address for future studies.

2) Errors linked to the radiosonde observations

Figure 6 shows the mean bias and standard deviation at each of the 10 sites, for each SAPHIR channel. The mean bias and standard deviation computed over the whole set are recalled at the right of each subfigure (ALL). Note that BAR only includes one radiosounding, resulting in a nil standard deviation for this site. Although the variability of the bias at SEY (10% of the database; Fig. 2) for C1 tends to increase the overall standard deviation for this channel, the SEY statistics for the other channels of SAPHIR are in good agreement with the dataset as a whole. The correction of surface temperature in radiosoundings performed on research vessels (*Baruna Jaya*, *Roger Revelle*) does not affect the global bias. The two sites with the greatest number of radiosonde observations are in good agreement for all channels. There is good overall agreement between the statistics for each single site and statistics for the dataset as a whole, and therefore no clear site-to-site dependence of the bias.

The drift of the radiosonde during an average ascent of 90-min duration may have a significant effect in this exercise. For this specific dataset, the mean horizontal drift is about 40 km, which corresponds to about four SAPHIR pixels. The RTM simulations assume a quasi-vertical ascent of the radiosonde and also a strong homogeneity of the water vapor field during the satellite overpass. To test the horizontal homogeneity, two different approaches were used to determine the SAPHIR-observed BT. One approach was to use the closest pixel to the radiosonde launch site. The other was to use the average of the 5 × 5 pixels surrounding the launch site, cleaned from diffusive scenes using the Hong et al. (2005a) method mentioned earlier. The results for both approaches are in Table 4. Note that the surrounding area was reduced to 3 × 5 pixels when the central pixel was located at the edge of the swath. Although the difference between mean biases calculated using one pixel versus the surrounding area are always less than 0.1 K (Table 4), it is important to account for the atmospheric variability in the area around the central pixel. For each channel, we define ε_v, the error due to local variability, as the mean standard deviation in the 15- or 25-pixel area around the central pixel for each channel of SAPHIR:

$$\varepsilon_v = \langle \sigma_{25\ \text{pixels}} \rangle \quad (\text{K}). \tag{4}$$

As mentioned in section 2b, two types of radiative bias corrections (NRBC and Vaisala) were applied to the daytime RS92 measurements. Figure 3 shows that 56% (44%) of the database was corrected with the Vaisala (NRBC) procedure. The two correction procedures were applied to daytime radiosonde observations only. Figure 7 shows how the two corrections differ with regard to the bias restricted to the daytime sample. The two methods produce corrections that differ by less than 0.3 K. For all channels but C1, the NRBC correction results in simulated BTs warmer than those simulated with Vaisala-corrected profiles.

Moreover, while the daytime subset was subject to an extensive correction procedure (see section 2b), the nighttime subset was corrected for temperature and time lag only. This distinction is made in Fig. 8 and is summarized in Table 4. Figure 8 shows that the two subsets present similar behavior for C2–C6 and that the larger outliers in C1 mainly belong to the daytime subset. For C1, there is a 0.96-K difference between the daytime and the nighttime subsets that may be due to a systematic nighttime moist bias in the CD radiosonde

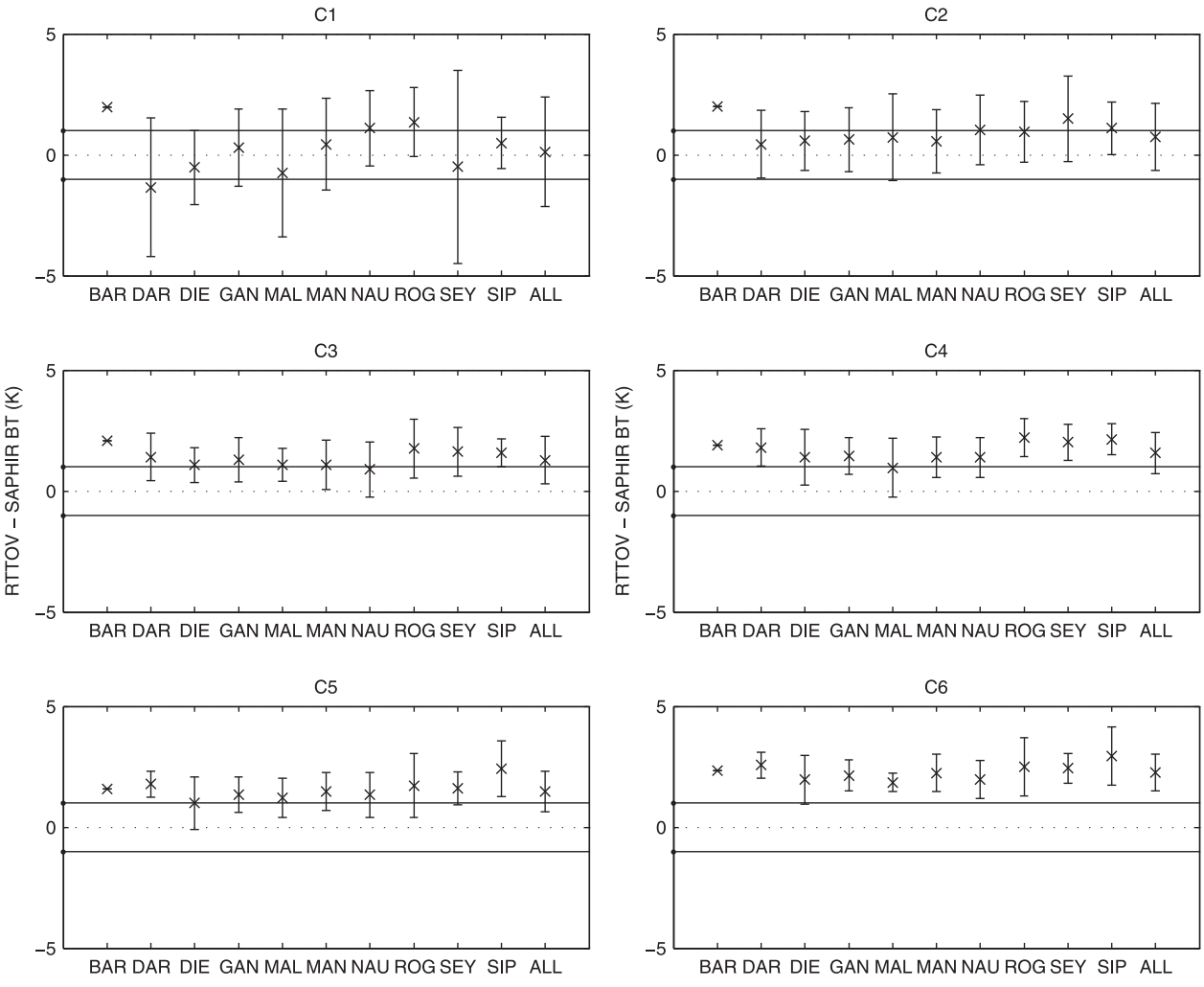

FIG. 6. RTTOV-10 minus SAPHIR mean bias and standard deviations for each CD site, using SAPHIR observations from a single pixel. The total mean bias is reported as "ALL."

observations, documented in Ciesielski et al. (2014). The bias difference between the two subsets (one pixel) is less than 0.7 K for C2 and less than 0.4 K for C3–C6. In addition, the correlation coefficients are similar for daytime and nighttime subsets for all channels but C1, for which the daytime subset correlation is 0.87 compared to 0.94 for the nighttime (Table 4).

Among the uncertainties affecting the radiosonde humidity observations, the production variability was not considered. The impact of the production variability is difficult to evaluate because of a lack of documentation on the changes in manufacturing processes. The evaluation of the model sensitivity to the production variability is also hardly feasible because the computation of this uncertainty creates important discontinuities in the input humidity profile.

The calibration uncertainty (section 2b) was corrected for GAN and MAL daytime observations only. To evaluate the sensitivity of the simulations to the calibration variability, RH input profiles were artificially modified according to the extreme values of the calibration uncertainty mentioned in section 2b. Table 5 summarizes the sensitivity of RTTOV-10 simulations to this change. As expected, a more (less) humid RH profile translates into a decrease (increase) in simulated BTs. The results for C1 are not representative, since the variability of changes for C1 is too high compared to the amplitude of the change in BT due to the input perturbation of RH. For C2–C6, the total sensitivity of the model is close to 1 K. Here we define a supplementary error $\varepsilon_{\mathrm{rsm}}$ describing the total sensitivity range of RTTOV-10 to the radiosonde calibration uncertainties:

$$\varepsilon_{\mathrm{rsm}} = \langle \mathrm{BT}_p - \mathrm{BT}_{\mathrm{ref}} \rangle_{\mathrm{RHdecrease}} - \langle \mathrm{BT}_p - \mathrm{BT}_{\mathrm{ref}} \rangle_{\mathrm{RHincrease}}, \quad (5)$$

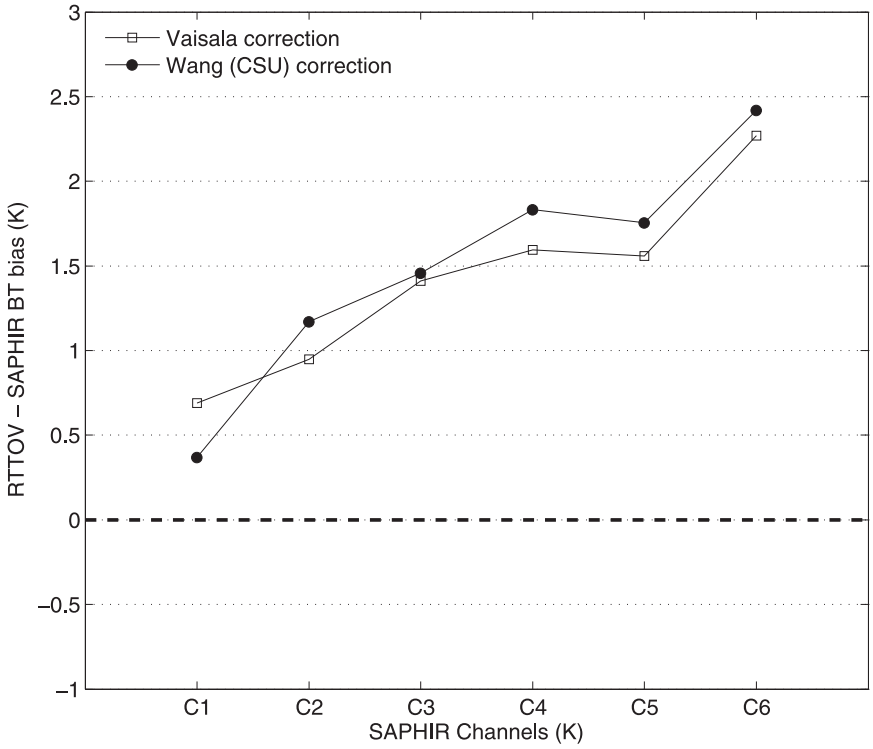

FIG. 7. Impact of Vaisala (open squares) and NRBC (Wang, Colorado State University) radiative corrections (black dots) on the RTTOV-10 minus SAPHIR BT bias (K) calculated from radiosonde observations performed during daytime only.

where BT_p are obtained after a perturbation of the RH profile, and BT_{ref} are associated with the unperturbed RH profiles. Since the radiosondes have the largest uncertainty in the upper troposphere, the impact on C1 is most certainly greater than 0 K, so we assigned to ε_{rsm} the same value as C2 as a realistic minimum. For channels C2–C6, the radiosonde daytime calibration error has a moderately higher impact (by <0.2 K) than the nighttime case. The magnitude of the daytime error is selected to be included in the total error calculation (see section 4c).

To put this study into perspective, we note that the MT team at CNES performed SAPHIR observations to RTTOV simulations using collocated ECMWF for clear-sky oceanic scenes. Those comparisons showed similar channel dependence on the bias to that shown in this work (section 4a).

3) ERRORS LINKED TO SAPHIR

Satellite observations near the 183.31-GHz water vapor absorption line can be used to detect strong convection, cold clouds, and precipitation (Hong et al. 2005a). According to Greenwald and Christopher (2002), the impact of cold (high level) clouds on satellite measurements equivalent to the SAPHIR C2 channel is to cool down the observed BT by 1.4 K on average. The impact of cold clouds should be greatest in the tropics. One can reasonably expect that scattering induced by lower-level and nonprecipitating clouds also would have a slight cooling effect on the observations. Some preliminary analyses on MHS data using cloud flags from IR sensors appears to show that clouds not detected by microwave-based cloud screening approaches could have a non-negligible impact, which could at least partially explain the channel dependency of the bias. A stringent RH filter was applied to the database in order to restrict to clear-sky scenes (section 2), but this filter might not be restrictive enough. The impact of clouds on the 183.31-GHz water vapor absorption line is not included in the present total error model, but the role of undetected clouds should not be forgotten in the discussion.

SAPHIR BTs scanned at nadir are warmer on average than the BTs scanned at the edges of swaths. This "limb effect" is described in Goldberg et al. (2001) and is accounted for in several studies: in Buehler et al. (2004), when verifying the consistency of radiosonde and MW satellite humidity observations; and in Karbou et al. (2005), when assessing the possibility to derive temperature and humidity profiles from AMSU-A and AMSU-B observations. On a single orbit, the mean BT difference

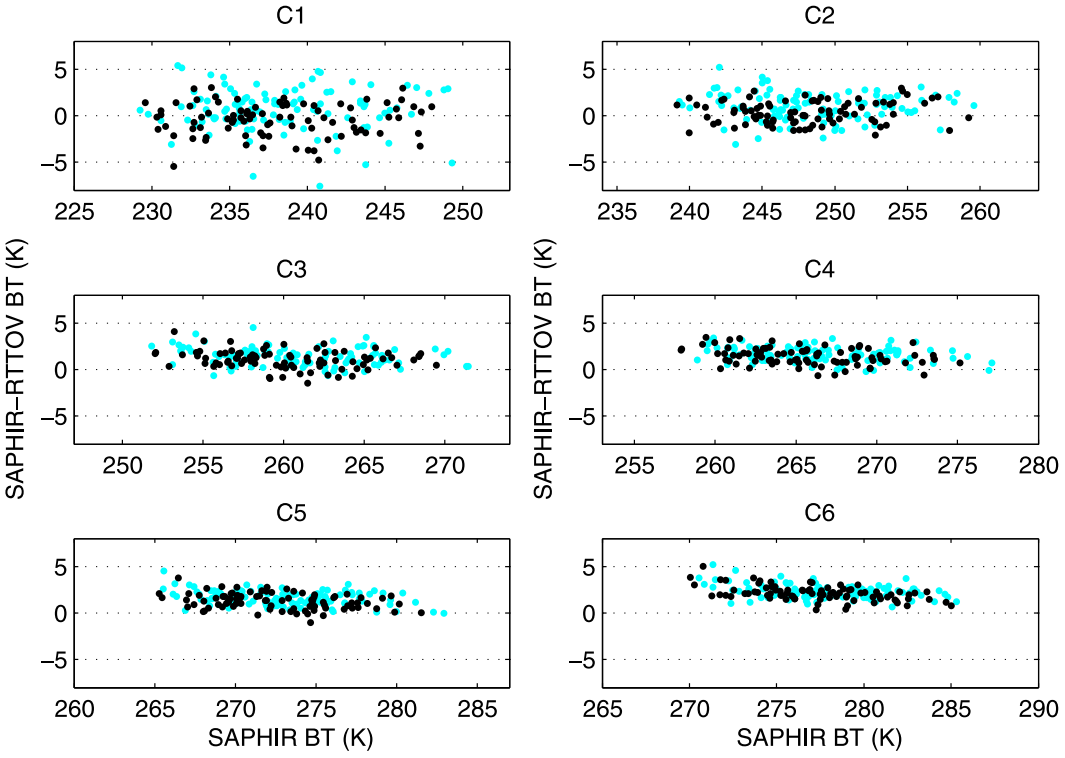

FIG. 8. RTTOV-10-simulated BTs vs SAPHIR L1A2 BTs (K). Blue and black markers refer to daytime and nighttime observations, respectively.

between nadir and edges of swaths in SAPHIR observations has been verified to range between 5 K for C1 and 4 K for C6 (not shown). Moreover, while substantial scan asymmetries have been observed for AMSU-B and MHS (Karbou et al. 2005; John et al. 2013), SAPHIR observations show virtually the same angle dependence on either side of the swath (N. Karouche, CNES, 2012, internal communication). The distributions of the mean biases for each channel according to the incidence viewing angles of SAPHIR are shown in Fig. 9. This figure shows no distinct angular dependence of the biases. The limb effect is accounted for in the BT simulations. Therefore, it will not be included in the total error model.

The actual shape of the instrument function is also accounted for in the model. The RT simulations performed for this work assumed top-hat transfer functions for SAPHIR channels. For SAPHIR, the actual shape of the instrument functions may show some very minor variations from this idealized shape at the edges, resulting in a negligible impact on the integrated observation (C. Goldstein, CNES, 2013, private communication).

The CNES report on SAPHIR in-flight performance (Karouche et al. 2012) shows very high stability in the hot load temperature used for in-flight calibration: the orbital temperature variations of the hot load are less than 1.5 K. In addition, comparisons with MHS (on *MetOp-A*) and the Advanced Technology Microwave Sounder (ATMS) on board the *Suomi National Polar-Orbiting Partnership* (*Suomi-NPP*) satellite (NASA and NOAA) have shown a good agreement between the instruments. SAPHIR C2, C3, and C5 were found to show "double differences" of

TABLE 5. Sensitivity of RTTOV-10 to the radiosonde calibration uncertainties.*

	Increase–decrease of f and o: f, o			
	$\langle BT_{ref} - BT_p \rangle$ (K), σ(K)			
	Nighttime		Daytime	
	1.04, 0.5	0.96, −0.5	1.05, 0.5	0.95, −0.5
C1	0.88, 0.43	−0.87, 0.24	1, 0.44	−1, 0.26
C2	0.58, 0.14	−0.6, 0.16	0.68, 0.15	−0.72, 0.17
C3	0.52, 0.1	−0.5, 0.11	0.6, 0.11	−0.64, 0.12
C4	0.5, 0.07	−0.52, 0.08	0.6, 0.08	−0.61, 0.09
C5	0.48, 0.05	−0.5, 0.05	0.6, 0.06	−0.6, 0.06
C6	0.46, 0.04	−0.48, 0.04	0.5, 0.05	−0.57, 0.06

*The sensitivity of simulated BT to the radiosonde calibration uncertainties are evaluated by applying a factor (f) and an offset value (o) to the radiosonde RH profile used as input to the model. The "perturbed' simulated BT (BT_p) is compared to the unperturbed or reference-simulated BT (BT_{ref}). Mean differences and standard deviations (σ) are reported for each channel. The f and o values refer to the extreme values of the radiosonde calibration uncertainty that differs between daytime and nighttime.

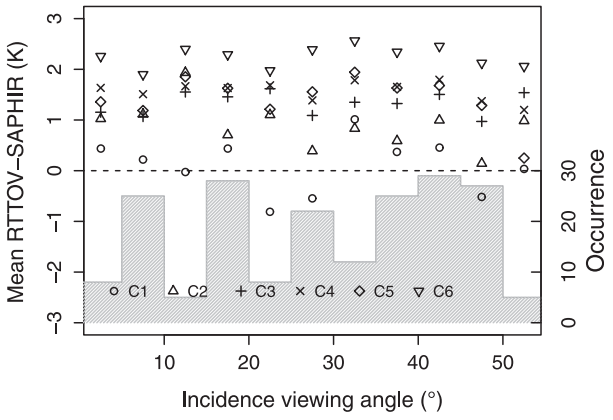

FIG. 9. Distribution of the mean differences between the simulated BTs and the SAPHIR BTs (K) according to the incidence viewing angles of SAPHIR. The number of points for each angle is indicated on the right axis.

0.2, 0.03, and 0.7 K with respect to *MetOp-A* MHS channels 3 (183.31 ± 1.0 GHz), 4 (183.31 ± 3.0 GHz), and 5 (190 GHz), respectively (Wilheit et al. 2013). Moreover, the mean double differences between SAPHIR and ATMS are 0.5, −1.3, −1.5, and −0.7 K for SAPHIR C2–ATMS 22 (183.31 ± 1.0 GHz), SAPHIR C3–ATMS 20 (183.31 ± 3.0 GHz), SAPHIR C4–ATMS 19 (183.31 ± 4.5 GHz), and SAPHIR C5–ATMS 18 (183.31 ± 7.0 GHz), respectively (Moradi 2014). (Note that differences in the channel specifications were accounted for in the double-difference approach, an indirect comparison between observations through a common reference set).

c. *Definition of the total uncertainty*

An accurate analysis of the bias between observations and simulations requires a comprehensive evaluation of the errors linked to each stage of the methodology (Immler et al. 2010). Considering a large number of observations or tests, stochastic variations of quantities that affect the measurements are generally considered as random errors and tend to a nil average with the increase of the size of the set of measurements. Systematic errors, for instance due to operating conditions, tend to result in a nonzero difference. An attempt to categorize the evaluated errors in terms of random or systematic has been made in Table 6. However, for this work, we choose to include all of the elementary terms in the global budget of error without a distinction of their nature. If we assume that the errors are additive and cannot be negatively correlated, then a pessimistic estimation of the total error is obtained from the absolute sum of the terms and gives the upper bound limit. The classical way is to assume that the errors are independent and uncorrelated, yielding to define the total error ε_T as the combination in quadrature of the five

TABLE 6. Numeric values of elementary errors (ε) in kelvins for each SAPHIR channel.*

ε (K), equation (#)	C1	C2	C3	C4	C5	C6	Category
ε_{is}, (1)	1.44	1.05	0.91	0.77	0.63	0.54	Random
ε_m, (2)	−0.81	−0.21	0.32	0.31	0.27	0.11	Systematic
ε_{O_3} (3)	—	0.50	—	—	—	0.05	Systematic
ε_v, (4)	1.12	0.90	0.84	0.78	0.76	0.74	Random
ε_{rsm}, (5)	**1.48**	1.48	1.23	1.17	1.08	1.02	Random
ε_T Absolute sum	3.23	3.72	3.30	3.03	2.74	2.46	
Quadratic sum	2.48	2.09	1.77	1.63	1.49	1.38	

* Term ε_{is} is the error linked to radiometric sensitivity (section 1). Term ε_m (section 2b) is the RTM error. Term ε_{O_3} is the error due to absorption by O_3 [section 3b(1)]. Term ε_v [section 3b(2)] depicts the local BT variability. Term ε_{rsm} [section 3b(2)] shows the sensitivity of RTTOV-10 to the radiosonde calibration uncertainty (nighttime case). The ε_{rsm} value for C1 is given in bold because it could not be directly estimated (see text). The categories random–systematic are included for discussion purposes.

estimated errors and to give a reasonable estimate of the global uncertainty (see Immler et al. 2010 for a discussion),

$$\varepsilon_T = (\varepsilon_{is}^2 + \varepsilon_m^2 + \varepsilon_{O_3}^2 + \varepsilon_v^2 + \varepsilon_{rsm}^2)^{1/2}. \quad (6)$$

This expression thus accounts for ε_{is}, linked to the radiometric sensitivity; ε_m, the estimated RTM error; ε_{O_3}, the error due to O_3 absorption; ε_v, the term reflecting the local atmospheric variability; and ε_{rsm}, the sensitivity of the fast RTM to the radiosonde calibration uncertainties. Both total errors (absolute and quadratic sums) are provided in Table 6, together with the summary of each error for each channel. From here on, we will assume that the elementary errors are independent, although we do acknowledge that some terms could be considered as linked (such as ε_m and ε_{O_3}).

The mean biases for each SAPHIR channel, with error bars accounting for the total uncertainty ε_T, are summarized in Fig. 10. The quantity ε_T is highest for C2 and decreases with distance from the 183.31-GHz line center. For all channels the calibration of the radiosondes is the main source of uncertainty. For C6, the confidence interval is 1.38 K and does not include the zero bias line, unlike the error bars for C1–C5. As seen from Table 6, the radiometric sensitivity ε_{is} and the atmospheric variability ε_v have the same contributions to the total error for all channels. The model error ε_m is the lowest contributor to the total error for all channels.

d. *Interpretation of the biases*

Based on the fact that intercomparisons of SAPHIR with MHS and ATMS show very good consistency of

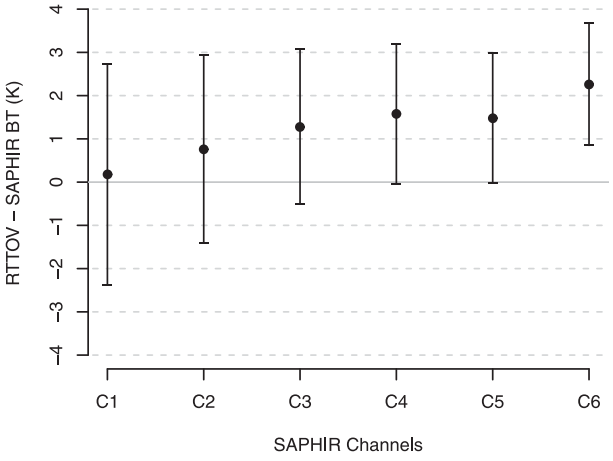

FIG. 10. Mean bias (K) with error bars referring to the total uncertainty ε_T defined in section 4c from the quadratic sum of the elementary errors in Table 6.

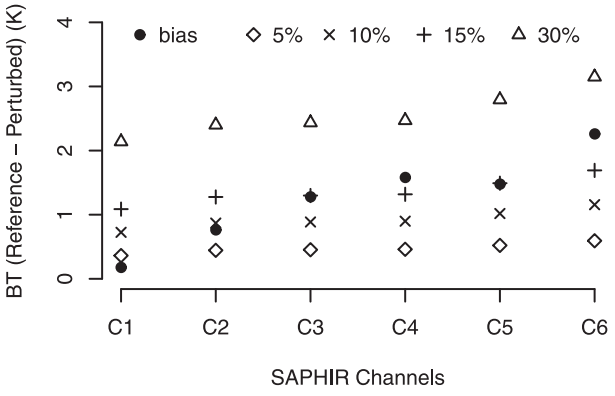

FIG. 11. Difference between the BT of a reference RH profile and the BT after a perturbation of the same profile. The perturbations of 5%, 10%, 15%, and 30% are relative values. The black dots correspond to the mean biases of SAPHIR given in Fig. 10.

the measurements (Wilheit et al. 2013; Moradi 2014), we do not believe that the channel-dependent bias is an instrumental issue. The systematic error sources listed in Table 6 do not show the same channel dependence as the biases. A simple sensitivity analysis was performed in order to determine whether the channel-dependent biases could be interpreted in terms of an altitude-dependent RH bias. Reference values of SAPHIR BTs were calculated from a representative tropical RH profile. These reference BTs were then compared to BTs computed using a set of perturbed RH profiles. Four perturbations are considered: 5%, 10%, 15%, and 30%. Figure 11 summarizes this sensitivity analysis and shows that, while C1 could be clearly considered as a bias-free channel, the biases of C2–C6 can be translated into a humidification of the atmosphere seen by SAPHIR, ranging between 5% and ~20%. This analysis seems to show that an altitude-dependent bias in the radiosonde measurements should not be totally ruled out. Indeed, the 2.26-K bias of C6 can be corrected if a 20% moistening were performed onto the RH profiles. However this conclusion should be further analyzed with respect to the very good quality of the CD upper-air measurements.

5. Summary and conclusions

In this study, a careful quality control procedure was applied to a tropical humidity radiosonde dataset. This dataset was used as input to a fast radiative transfer model in order to simulate BTs observed by the SAPHIR instrument on board Megha-Tropiques and to evaluate its performance. The simulated-minus-observed BTs indicate an overall warm bias in the simulations that increases with distance from line center (0.12 K at C1 to 2.3 K at C6) and a strong linearity between simulations and observations.

The sources of uncertainties and/or errors can be associated with the measurements themselves (the SAPHIR sounder and the radiosoundings) and with the methodology of evaluation that uses an RTM. Overall, five elementary sources classified as random or systematic (see Table 6) have been evaluated numerically. Assuming that all the terms are uncorrelated, they are quadratically summed to estimate a total uncertainty, interpreted as a confidence interval around the bias. The total uncertainty is widest for C1 and C2 and decreases with distance from the 183.31-GHz line center. The channel-dependent feature of the model-observed bias can be discussed with respect to these uncertainties:

- The instrumental sensitivity, which gives the accuracy of the measurements and could be considered as a random source of error. Intercalibration efforts at NASA and NOAA on MHS–*MetOp-A* and ATMS–*Suomi-NPP* (Wilheit et al. 2013; Moradi 2014) appear to rule out an instrumental issue specific to SAPHIR (except maybe for C6), since all three sounders show very consistent measurements.
- The variations in BT simulations, are linked to the choice of RTM used within the comparison; this would be a systematic error. Comparisons between RTTOV-10 and two LBL models with different spectroscopic specifications (ARTS and MonoRTM) do not explain the increasing difference. It is also possible that the difference between the idealized top-hat and the actual shape of the instrument function can create a discrepancy between simulations and observations. However, based on the information provided by CNES, the SAPHIR instrument response functions are assumed to be very close to the top-hat ideal.
- The impact of ozone lines in BT simulations near the 183.31-GHz line; also a systematic error that should be

accounted for mainly when considering simulations at 184 GHz (O_3 absorption), but that is negligible at other frequencies.
- The local atmospheric variability in SAPHIR observations, a random error. There is possible contamination by thin clouds that have not been removed by the method applied here, which was designed to remove deep convective overshoots and cirrus anvil cloud. The role of clouds requires further investigation.
- The sensitivity of RTTOV-10 to calibration uncertainties in radiosonde RH observations, which could be interpreted as a random error. This is the major source of uncertainty in the global error budget. Evaluation of the impact of the radiosonde production variability would require the manufacturer to provide information about the changes in manufacturing processes and calibration that can occur over time.

Finally, among the other sources of uncertainties that have not been evaluated numerically, some are linked to the spectroscopic input to the RT models, such as the absorption by N_2 and the impact of the water vapor continuum, which might affect low-peaking observations. For instance, the impact of uncertainties in the spectroscopic parameters associated with the 183.31-GHz line and other water vapor lines (e.g., air- and self-broadened line widths, temperature dependences of these widths) should be the object of a specific evaluation. Note, however, that preliminary work on evaluating the amplitude of these spectroscopic uncertainties suggests that this will not explain the observed biases.

A sensitivity analysis on a test tropical RH profile indicates that the channel-dependent bias could be interpreted in terms of a 15%–20% relative perturbation. Despite the strong quality control applied to this radiosonde dataset (Ciesielski et al. 2014), we might still suspect biases in the radiosonde RH profiles. However, we do note that complementary studies exploring ECMWF or National Centers for Environmental Prediction (NCEP) profiles or other corrected radiosonde measurements (such as those available from Atmospheric Radiation Measurement Program sites) show the very same behavior for other MW sounders with close frequency channels. If there is an issue with RH profile biases, it is not unique to this CD radiosonde dataset.

Acknowledgments. This work is funded by the French National Space Center (CNES). The authors thank Tom Wilheit for the fruitful discussions about SAPHIR calibration. We wish to thank the NWP SAF team for its help with the RTTOV model, and we acknowledge specifically Peter Rayer and James Hocking.

The radiosonde data were collected as part of DYNAMO, which was sponsored by NSF, NOAA, ONR, DOE, NASA, JAMSTEC, and Indian and Australian funding agencies. For the radiosonde observations performed at the GAN site during the CINDY/DYNAMO campaign, acknowledgements are directed to the U.S. Department of Energy as part of the Atmospheric Radiation Measurement (ARM) Climate Research Facility. The involvement of the NSF-sponsored National Center for Atmospheric Research (NCAR) Earth Observing Laboratory (EOL) is acknowledged. The data are archived at the DYNAMO Data Archive Center maintained by NCAR EOL. Together with the CINDY/DYNAMO science team, we acknowledge particularly Junhong Wang, Richard H. Johnson, Paul E. Ciesielski, and Kunio Yoneyama.

Part of this research was carried out at the Jet Propulsion Laboratory, California Institute of Technology, under a contract with the National Aeronautics and Space Administration. Reference herein to any specific commercial product, process, or service by trade name, trademark, manufacturer, or otherwise, does not constitute or imply its endorsement by the U.S. government or the Jet Propulsion Laboratory, California Institute of Technology. MonoRTM is a LBL RTM developed by Atmospheric and Environmental Research (AER). The model is publicly available and may be downloaded (from http://rtweb.aer.com). Thanks to the ARTS community (http://www.sat.ltu.se/arts/) for providing the ARTS radiative transfer model.

This work also benefited from discussions with Bruno Picard from Collecte Localisation Satellite (CLS, CNES/IFREMER/ARDIAN), who worked on the comparisons between ECMWF and SAPHIR. Finally, the three anonymous reviewers are thanked for their in-depth comments on the manuscript.

REFERENCES

Aires, F., C. Prigent, F. Bernardo, C. Jiménez, R. Saunders, and P. Brunel, 2011: A Tool to Estimate Land-Surface Emissivities at Microwave frequencies (TELSEM) for use in numerical weather prediction. *Quart. J. Roy. Meteor. Soc.,* **137,** 690–699, doi:10.1002/qj.803.

Berrisford, P., D. Dee, K. Fielding, M. Fuentes, P. Kållberg, S. Kobayashi, and S. Uppala, 2009: The ERA-Interim archive. Version 1, ERA Report Series 1, ECMWF Tech. Rep., 16 pp. [Available online at http://old.ecmwf.int/publications/library/ecpublications/_pdf/era/era_report_series/RS_1.pdf.]

Brogniez, H., R. Roca, and L. Picon, 2006: A clear-sky radiance archive from Meteosat "water vapor" observations. *J. Geophys. Res.,* **111,** D21109, doi:10.1029/2006JD007238.

——, P.-E. Kirstetter, and L. Eymard, 2013: Expected improvements in the atmospheric humidity profile retrieval using the Megha-Tropiques microwave payload. *Quart. J. Roy. Meteor. Soc.,* **139,** 842–851, doi:10.1002/qj.1869.

Buehler, S. A., and V. O. John, 2005: A simple method to relate microwave radiances to upper tropospheric humidity. *J. Geophys. Res.,* **110,** D02110, doi:10.1029/2004JD005111.

——, M. Kuvatov, V. O. John, U. Leiterer, and H. Dier, 2004: Comparison of microwave satellite humidity data and radiosonde profile: A case study. *J. Geophys. Res.,* **109,** D13103, doi:10.1029/2004JD004605.

——, P. Eriksson, T. Kuhn, A. von Engeln, and C. Verdes, 2005: ARTS, the Atmospheric Radiative Transfer Simulator. *J. Quant. Spectrosc. Radiat. Transfer,* **91,** 65–93, doi:10.1016/j.jqsrt.2004.05.051.

——, N. Courcoux, and V. O. John, 2006: Radiative transfer calculations for a passive microwave satellite sensor: Comparing a fast model and a line-by-line model. *J. Geophys. Res.,* **111,** D20304, doi:10.1029/2005JD006552.

Cadeddu, M. P., V. H. Payne, S. A. Clough, K. E. Cady-Pereira, and J. C. Liljegren, 2007: Effect of the oxygen line-parameter modeling on temperature and humidity retrievals from ground-based microwave radiometers. *IEEE Trans. Geosci. Remote Sens.,* **45,** 2216–2223, doi:10.1109/TGRS.2007.894063.

Chen, Y., Y. Han, P. Van Delst, and F. Weng, 2010: On water vapor Jacobian in fast radiative transfer model. *J. Geophys. Res.,* **115,** D12303, doi:10.1029/2009JD013379.

Ciesielski, P. E., P. H. Haertel, R. H. Johnson, J. Wang, and S. Loehrer, 2012: Developing high-quality field program sounding datasets. *Bull. Amer. Meteor. Soc.,* **93,** 325–336, doi:10.1175/BAMS-D-11-00091.1.

——, and Coauthors, 2014: Quality-controlled upper-air sounding dataset for DYNAMO/CINDY/AMIE: Development and corrections. *J. Atmos. Oceanic Technol.,* **31,** 741–764, doi:10.1175/JTECH-D-13-00165.1.

Cimini, D., F. Nasir, E. R. Westwater, V. H. Payne, D. D. Turner, E. J. Mlawer, M. L. Exner, and M. P. Cadeddu, 2009: Comparison of ground-based millimeter wave observations in the Arctic winter. *IEEE Trans. Geosci. Remote Sens.,* **47,** 3098, doi:10.1109/TGRS.2009.2020743.

Clough, S. A., Y. Beers, J. P. Klein, and L. S. Rothman, 1973: Dipole moment of water from Stark measurements of H_2O, HDO and D_2O. *J. Chem. Phys.,* **59,** 2254–2259, doi:10.1063/1.1680328.

——, M. W. Shephard, E. Mlawer, J. S. Delamere, M. Iacono, K. E. Cady-Pereira, S. Boukabara, and P. D. Brown, 2005: Atmospheric radiative transfer modeling: A summary of the AER codes. *J. Quant. Spectrosc. Radiat. Transfer,* **91,** 233–244, doi:10.1016/j.jqsrt.2004.05.058.

Desbois, M., M. Capderou, L. Eymard, R. Roca, N. Viltard, M. Viollier, and N. Karouche, 2007: *Megha-Tropiques*: Un satellite hydrométéorologique franco-indien. *Meteorologie,* **57,** 19–27, doi:10.4267/2042/18185.

English, S. J., and T. J. Hewison, 1998: A fast generic millimeter-wave emissivity model. *Microwave Remote Sensing of the Atmosphere and Environment,* T. Hayasaka et al., Eds., International Society for Optical Engineering (SPIE Proceedings, Vol. 3503), 288, doi:10.1117/12.319490.

Eriksson, P., S. A. Buehler, C. P. Davis, C. Emde, and O. Lemke, 2011: ARTS, the atmospheric radiative transfer simulator, version 2. *J. Quant. Spectrosc. Radiat. Transfer,* **112,** 1551–1558, doi:10.1016/j.jqsrt.2011.03.001.

Eymard, L., and Coauthors, 2002: The SAPHIR humidity sounder. Notes des Activités Instrumentales de l'IPSL 24, 17 pp.

Fetzer, E. J., and Coauthors, 2003: AIRS/AMSU/HSB validation. *IEEE Trans. Geosci. Remote Sens.,* **41,** 418–431, doi:10.1109/TGRS.2002.808293.

——, B. H. Lambrigstenm, A. Eldering, H. H. Aumann, and M. T. Chahine, 2006: Biases in total precipitable water vapor climatologies from the Atmospheric Infrared Sounder and Advanced Microwave Scanning Radiometer. *J. Geophys. Res.,* **111,** D09S16, doi:10.1029/2005JD006598.

Gohil, B. S., R. Gairola, A. Mathur, A. Varma, C. Mahesh, R. Gangwar, and P. Pal, 2013: Algorithms for retrieving geophysical parameters from the MADRAS and SAPHIR sensors of the Megha-Tropiques satellite: Indian scenario. *Quart. J. Roy. Meteor. Soc.,* **139,** 954–963, doi:10.1002/qj.2041.

Goldberg, M. D., D. S. Crosby, and L. Zhou, 2001: The limb adjustment of AMSU-A observations: Methodology and validation. *J. Appl. Meteor.,* **40,** 70–83, doi:10.1175/1520-0450(2001)040<0070:TLAOAA>2.0.CO;2.

Greenwald, T. J., and S. A. Christopher, 2002: Effect of cold clouds on satellite measurements near 183 GHz. *J. Geophys. Res.,* **107,** 4170, doi:10.1029/2000JD000258.

Hong, G., G. Heygster, J. Miao, and K. Kunzi, 2005a: Detection of tropical deep convective clouds from AMSU-B water vapor channels measurements. *J. Geophys. Res.,* **110,** D05205, doi:10.1029/2004JD004949.

——, ——, ——, and ——, 2005b: Sensitivity of microwave brightness temperatures to hydrometeors in a tropical deep convective cloud system at 89–190 GHz. *Radio Sci.,* **40,** RS4003, doi:10.1029/2004RS003129.

Immler, F. J., J. Dykema, T. Gardiner, D. N. Whiteman, P. W. Thorne, and H. Vömel, 2010: Reference Quality Upper-Air Measurements: Guidance for developing GRUAN data products. *Atmos. Meas. Tech.,* **3,** 1217–1231, doi:10.5194/amt-3-1217-2010.

John, V. O., and S. A. Buehler, 2004: The impact of ozone lines on AMSU-B radiances. *Geophys. Res. Lett.,* **31,** L21108, doi:10.1029/2004GL021214.

——, G. Holl, R. P. Allan, S. A. Buehler, D. E. Parker, and B. J. Soden, 2011: Clear-sky biases in satellite infrared estimates of upper tropospheric humidity and its trends. *J. Geophys. Res.,* **116,** D14108, doi:10.1029/2010JD015355.

——, ——, N. Atkinson, and S. A. Buehler, 2013: Monitoring scan asymmetry of microwave humidity sounding channels using simultaneous all angle collocations (SAACs). *J. Geophys. Res. Atmos.,* **118,** 1536–1545, doi:10.1002/jgrd.50154.

Karbou, F., F. Aires, C. Prigent, and L. Eymard, 2005: Potential of Advanced Microwave Sounding Unit-A (AMSU-A) and AMSU-B measurements for atmospheric temperature and humidity profiling over land. *J. Geophys. Res.,* **110,** D07109, doi:10.1029/2004JD005318.

Karouche, N., C. Goldstein, A. Rosak, C. Malassingne, and G. Raju, 2012: MEGHA-TROPIQUES satellite mission: In flight performance results. *2012 IEEE International Geoscience and Remote Sensing Symposium: Proceedings,* IEEE, 4684–4687, doi:10.1109/IGARSS.2012.6350420.

Kottayil, A., S. A. Buehler, V. John, L. Miloshevich, M. Milz, and G. Holl, 2012: On the importance of Vaisala RS92 radiosonde humidity corrections for a better agreement between measured and modeled satellite radiances. *J. Atmos. Oceanic Technol.,* **29,** 248–259, doi:10.1175/JTECH-D-11-00080.1.

Lanzante, J. R., and G. E. Gahrs, 2000: The "clear-sky bias" of TOVS upper-tropospheric humidity. *J. Climate,* **13,** 4034–4041, doi:10.1175/1520-0442(2000)013<4034:TCSBOT>2.0.CO;2.

Liebe, H. J., 1989: MPM—An atmospheric millimeter-wave propagation model. *Int. J. Infrared Millimeter Waves,* **10,** 631–650, doi:10.1007/BF01009565.

——, P. W. Rosenkranz, and G. A. Hufford, 1992: Atmospheric 60-GHz oxygen spectrum: New laboratory measurements and line parameters. *J. Quant. Spectrosc. Radiat. Transfer,* **48,** 629–643, doi:10.1016/0022-4073(92)90127-P.

——, G. A. Hufford, and M. G. Cotton, 1993: Propagation modeling of moist air and suspended water/ice particles at frequencies below 1000 GHz. Atmospheric propagation effects through natural and man-made obscurants for visible to mm-wave radiation, AGARD Conference Proceedings 542, AGARD-CP-542, 3-1–3-10. [Available online at http://www.dtic.mil/dtic/tr/fulltext/u2/a276919.pdf.]

Miloshevich, L. M., A. Paukkunen, H. Vömel, and S. Oltmans, 2004: Development and validation of a time lag correction for Vaisala radiosonde humidity measurements. *J. Atmos. Oceanic Technol.,* **21,** 1305–1327, doi:10.1175/1520-0426(2004)021<1305:DAVOAT>2.0.CO;2.

——, H. Vömel, D. N. Whiteman, B. M. Lesht, F. J. Schmidlin, and F. Russo, 2006: Absolute accuracy of water vapor measurements from six operational radiosonde types launched during AWEX-G and implications for AIRS validation. *J. Geophys. Res.,* **111,** D09S10, doi:10.1029/2005JD006083.

——, ——, D. N. Whitman, and T. Leblanc, 2009: Accuracy assessment and correction of Vaisala RS92 radiosonde water vapor measurements. *J. Geophys. Res.,* **114,** D11305, doi:10.1029/2008JD011565.

Mlawer, E. J., V. H. Payne, J.-L. Moncet, J. S. Delamere, M. J. Alvarado, and D. C. Tobin, 2012: Development and evaluation of the MT_CKD model of continuum absorption. *Philos. Trans. Roy. Soc. London,* **A370,** 2520–2556, doi:10.1098/rsta.2011.0295.

Moradi, I., 2014: Inter-calibration of observations from SAPHIR and ATMS instruments. *GSICS Quarterly,* Vol. 8, No. 1, GSICS Coordination Center, College Park, MD, 1–2, doi:10.7289/V55H7D64.

——, B. Soden, R. Ferraro, P. Arkin, and H. Vömel, 2013: Assessing the quality of humidity measurements from global operational radiosonde sensors. *J. Geophys.Res. Atmos.,* **118,** 8040–8053, doi:10.1002/jgrd.50589.

Nash, J., T. Oakley, H. Vömel, and L. Wei, 2011: WMO intercomparison of high quality radiosonde systems. IOM Rep. 107, WMO/TD-1580, 238 pp. [Available online at http://www.wmo.int/pages/prog/www/IMOP/publications/IOM-107_Yangjiang/IOM-107_Yangjiang.zip.]

Payne, V. H., J. S. Delamere, K. E. Cady-Pereira, R. R. Gamache, J.-L. Moncet, E. J. Mlawer, and S. A. Clough, 2008: Air-broadened half-widths of the 22- and 183-GHz water-vapor lines. *IEEE Trans. Geosci. Remote Sens.,* **46,** 3601–3617, doi:10.1109/TGRS.2008.2002435.

——, E. J. Mlawer, K. E. Cady-Pereira, and J.-L. Moncet, 2011: Water vapor continuum absorption in the microwave. *IEEE Trans. Geosci. Remote Sens.,* **49,** 2194–2208, doi:10.1109/TGRS.2010.2091416.

Peixoto, J. P., and A. H. Oort, 1996: The climatology of relative humidity in the atmosphere. *J. Climate,* **9,** 3443–3463, doi:10.1175/1520-0442(1996)009<3443:TCORHI>2.0.CO;2.

Prigent, C., F. Aires, and W. Rossow, 2006: Land surface microwave emissivities over the globe for a decade. *Bull. Amer. Meteor. Soc.,* **87,** 1573–1584, doi:10.1175/BAMS-87-11-1573.

Prigent C., E. Jaumouille, F. Chevallier, and F. Aires, 2008: A parameterization of the microwave land surface emissivity between 19 and 100 GHz, anchored to satellite-derived estimates. *IEEE Trans. Geosci. Remote Sens.,* **46,** 344–352, doi:10.1109/TGRS.2007.908881.

Roca, R., and Coauthors, 2010: On the water and energy cycles in the tropics. *C. R. Geosci.,* **342,** 390–402, doi:10.1016/j.crte.2010.01.003.

Rosenkranz, P. W., 1993: Absorption of microwaves by atmospheric gases. *Atmospheric Remote Sensing by Microwave Radiometry,* M. A. Janssen, Ed., Wiley Series in Remote Sensing and Image Processing, Vol. 6, John Wiley and Sons, 37–90.

——, 1998: Water vapor microwave continuum absorption: A comparison of measurements and models. *Radio Sci.,* **33,** 919–928, doi:10.1029/98RS01182; Corrigendum, **34,** 1025, doi:10.1029/1999RS900020.

Saunders, R., M. Matricardi, and P. Brunel, 1999: A fast radiative transfer model for assimilation of satellite radiance observations—RTTOV-5. ECMWF Research Dept. Tech. Memo. 282, 29 pp. [Available online at http://old.ecmwf.int/publications/library/ecpublications/_pdf/tm/001-300/tm282.pdf.]

——, and Coauthors, 2012: RTTOV-10 science and validation report. NWP SAF Doc. NWPSAF-MO-TV-023, Version 1.11, 31 pp. [Available online at http://nwpsaf.eu/deliverables/rtm/docs_rttov10/rttov10_svr_1.11.pdf.]

Seidel, D. J., and Coauthors, 2009: Reference upper-air observations for climate: Rationale, progress, and plans. *Bull. Amer. Meteor. Soc.,* **90,** 361–369, doi:10.1175/2008BAMS2540.1.

Spencer, R. W., and W. D. Braswell, 1997: How dry is the tropical free troposphere? Implications for global warming theory. *Bull. Amer. Meteor. Soc.,* **78,** 1097–1106, doi:10.1175/1520-0477(1997)078<1097:HDITTF>2.0.CO;2.

Student, 1908: The probable error of a mean. *Biometrika,* **6,** 1–25.

Tobin, D., and Coauthors, 2006: Atmospheric Radiation Measurement site atmospheric state best estimates for Atmospheric Infrared Sounder temperature and water vapor retrieval validation. *J. Geophys. Res.,* **111,** D09514, doi:10.1029/2005JD006103.

Vömel, H., and Coauthors, 2007: Radiation dry bias of the Vaisala RS92 humidity sensor. *J. Atmos. Oceanic Technol.,* **24,** 953–963, doi:10.1175/JTECH2019.1.

Wang, J., L. Zhang, A. Dai, F. Immler, M. Sommer, and H. Voemel, 2013: Radiation dry bias correction of Vaisala RS92 humidity data and its impacts on historical radiosonde data. *J. Atmos. Oceanic Technol.,* **30,** 197–214, doi:10.1175/JTECH-D-12-00113.1.

Wilheit, T., H. Brogniez, S. Datta, W. Liinwood Jones, V. Payne, E. Stocker, and J. Wang, 2013: The use of SAPHIR on Megha-Tropiques for intercalibration of polar-orbiting microwave water vapor sounders. *2013 EUMETSAT Meteorological Satellite Conf./ 19th American Meteorological Society Satellite Meteorology, Oceanography, and Climatology Conf.,* Vienna, Austria, EUMETSAT and Amer. Meteor. Soc., 272. [Available online at www.eumetsat.int/website/wcm/idc/idcplg?IdcService=GET_FILE&dDocName=PDF_CONF_2013_ABSTRACTS&RevisionSelectionMethod=LatestReleased&Rendition=Web.]

Yoneyama, K., M. Hanyu, F. Yoshiura, S. Sueyoshi, and M. Katsumat, 2002: Radiosonde observation from the ship in the tropical region. *Report of the Japan Agency for Marine-Earth Science and Technology (JAMSTECR),* No. 45, JAMSTEC, Yokosuka, Japan, 31–39. [Available online at http://www.godac.jamstec.go.jp/catalog/data/doc_catalog/media/JAM12-1_all.pdf.]

Yue, Q., E. Fetzer, B. H. Kahn, S. Wang, G. Mariponm, A. Guillaume, and B. Wilson, 2013: Cloud-state-dependent sampling in AIRS observations based on *CloudSat* cloud classification. *J. Climate,* **26,** 8357–8377, doi:10.1175/JCLI-D-13-00065.1.